ACS NANO

www.acsnano.org

ARTICLE

On-Wire Design of Axial Periodic Halide Perovskite Superlattices for High-Performance Photodetection

Qihang Lv,[#] Xia Shen,[#] Xuyang Li,[#] You Meng, Kin Man Yu, Pengfei Guo,[*] Liantuan Xiao,[*] Johnny C. Ho, Xidong Duan,[*] and Xiangfeng Duan

Cite This: *ACS Nano* 2024, 18, 18022−18035

Read Online

ACCESS | Metrics & More | Article Recommendations | Supporting Information

ABSTRACT: **Precise synthesis of all-inorganic lead halide perovskite nanowire heterostructures and superlattices with designable modulation of chemical compositions is essential for tailoring their optoelectronic properties. Nevertheless, controllable synthesis of perovskite nanostructure heterostructures remains challenging and underexplored to date. Here, we report a rational strategy for wafer-scale synthesis of one-dimensional periodic $CsPbCl_3/CsPbI_3$ superlattices. We show that the highly parallel array of halide perovskite nanowires can be prepared roughly as horizontally guided growth on an *M*-plane sapphire. A periodic patterning of the sapphire substrate enables position-selective ion exchange to obtain highly periodic $CsPbCl_3/CsPbI_3$ nanowire superlattices. This patterning is further confirmed by micro-photoluminescence investigations, which show that two separate band-edge emission peaks appear at the interface of a $CsPbCl_3/CsPbI_3$ heterojunction. Additionally, compared with the pure $CsPbCl_3$ nanowires, photodetectors fabricated using these periodic heterostructure nanowires exhibit superior photoelectric performance, namely, high I_{ON}/I_{OFF} ratio (10^4), higher responsivity (49 A/W), and higher detectivity (1.51×10^{13} Jones). Moreover, a spatially resolved visible image sensor based on periodic nanowire superlattices is demonstrated with good imaging capability, suggesting promising application prospects in future photoelectronic imaging systems. All these results based on the periodic $CsPbCl_3/CsPbI_3$ nanowire superlattices provides an attractive material platform for integrated perovskite devices and circuits.**

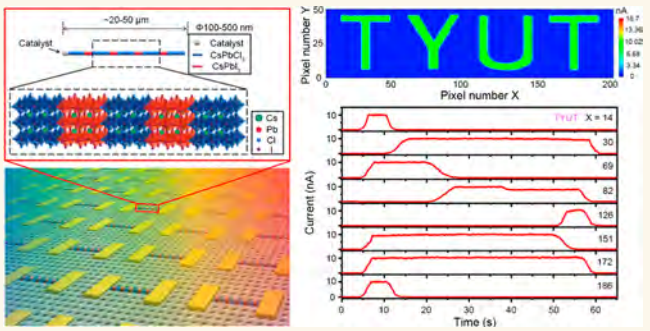

KEYWORDS: *on-wire bandgap design, perovskite nanowire superlattices, horizontal guided growth, heterostructure nanowire arrays, high-performance photodetection*

INTRODUCTION

All-inorganic lead halide perovskite nanowires are considered to be a candidate material for integrated photonics owing to their unique chemical and physical properties.[1−13] The development of perfect ways to engineer lead halide perovskite structures with controllable bandgaps and optoelectronic properties is an active research topic in materials science and technology, which may lead to promising applications in the future.[14−27] Especially, bandgap engineering along single-perovskite complex structures could provide an effective way for constructing highly integrated,[28−37] low power consumption, and miniaturized optoelectronic devices, including all-optical switches,[38,39] light-emitting diodes,[40,41] optical logic gates,[42] lasers,[35,36] solar cells,[43,44] and photodetectors.[45−49]

Nanowires with predictable and controllable optoelectrical properties[50−52] can be rationally constructed by complex compositional modulated processes, for example, multistep ion exchange,[37,53] ion doping,[54] and restricted phase transformation process.[34,55,56] So far, a large number of semiconductor heterojunction nanowires have been reported,[57−59] not only for traditional group II−VI and III−V semiconductors but also for the freshly emerged promising perovskite materials. Some examples include CdSe−ZnSe heterostructure nanowires,[60] $CdS/CdS:SnS_2$ superlattice nanowires,[61] CdS−Ag_2S superlattice nanorods,[62] Si-SiGe superlattice nanowires,[63]

Received: April 19, 2024
Revised: June 13, 2024
Accepted: June 14, 2024
Published: June 27, 2024

https://doi.org/10.1021/acsnano.4c05205
ACS Nano 2024, 18, 18022−18035

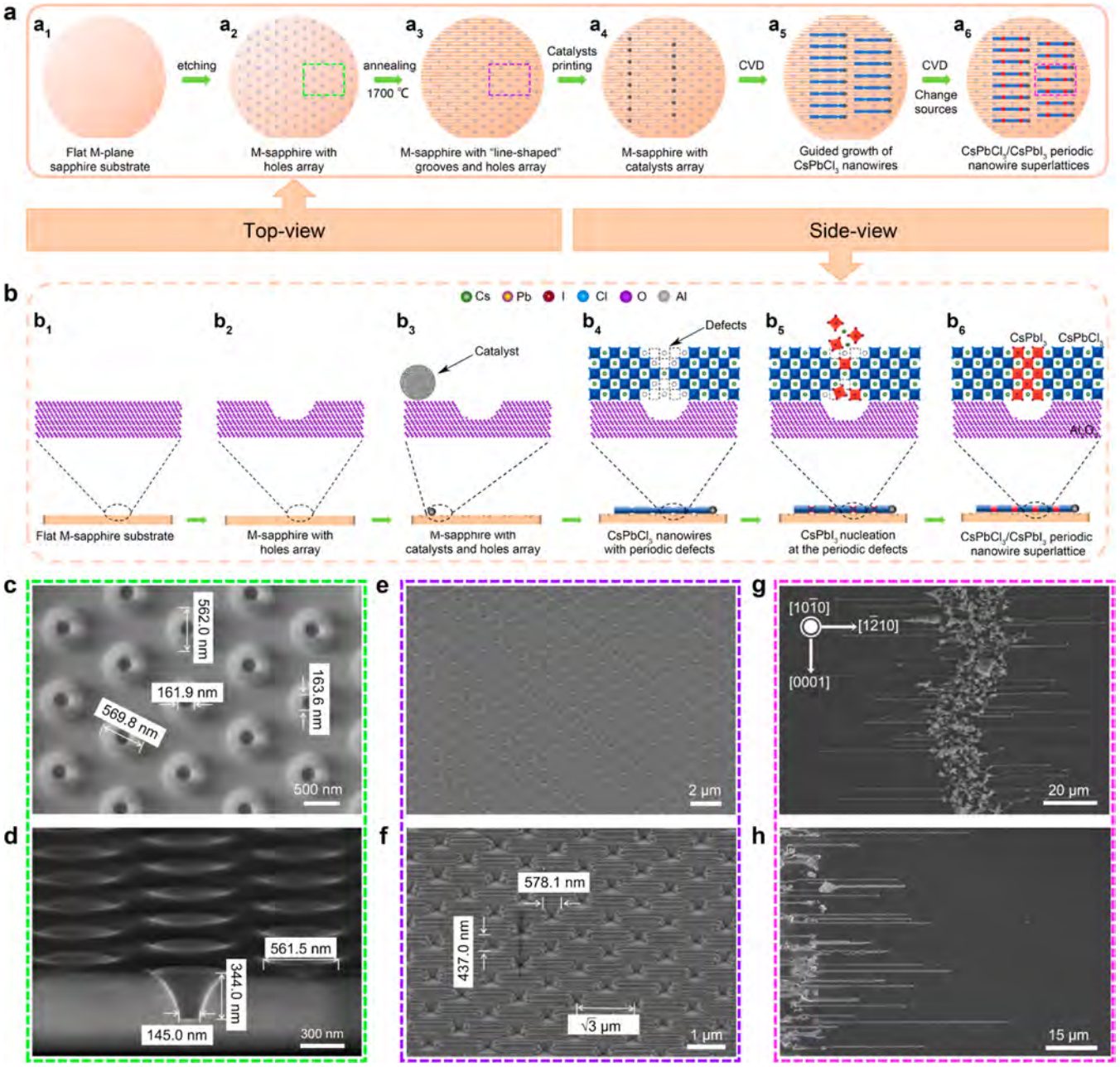

Figure 1. Fabrication process and cross-sectional schematic diagram and corresponding SEM images of the $CsPbCl_3/CsPbI_3$ periodic nanowire superlattices on a *M*-plane sapphire. (a) Top view fabrication process and (b) side view cross-sectional growth model of the $CsPbCl_3/CsPbI_3$ periodic nanowire superlattices. (c,d) Top and side view SEM images of the prefabricated *M*-plane sapphire with hole arrays. (e,f) Low- and high-resolution SEM images of the prefabricated sapphire substrate after annealing. (g,h) Two typical SEM images of the guided growth periodic $CsPbCl_3/CsPbI_3$ nanowire superlattice array on the prefabricated *M*-plane sapphire.

GaAs-GaP superlattice structures,[64] GaAs/GaAsSb nanowires superlattice,[65] InAs−InP heterostructures,[66] etc. Many recent studies on perovskite nanostructures have also been reported,[67−69] including spatially resolved $CsPbX_3$ (X = Cl, Br, I, or alloys) heterojunction nanowires,[37] local phase transition of halide perovskite $CsSnI_3$ nanowires from yellow phase to black phase,[34] controllability of phase propagation on an individual ultralong $CsPbI_3$ nanowires,[55] $CsPbCl_{3-3x}Br_{3x}$ perovskite nanowires,[35] $CsPbI_3/CsPbI_{3-3x}Br_{3x}$ epitaxial perovskite heterojunctions,[70] composition gradient $CsPbBr_xI_{3-x}$ nanowires,[36] $CsPbBr_3/CsPbCl_{1.1}Br_{1.9}$ heterostructures,[71] $CsPbCl_3/CsPbBr_3$ heterostructure by solid-state ion exchange,[53] etc. These specific perovskite heterostructures have been used in photodetector devices and exhibited excellent photoelectric performance, for example, the $MAPbBr_3$−$MAPbI_3$ microwire lateral heterojunction photodetector based on a high performance with a responsivity and detectivity of 1207 A/W and 2.78×10^{13} Jones,[47] respectively, and gradient perovskite single-crystalline microwire arrays from $MAPbCl_3$ to $MAPbI_3$ for a photodetector with responsivity over 10^3 A/W and detectivity over 10^{15} Jones.[21] Although the component modulation of semiconductor nanowires has been widely investigated, many studies rely on accidental nucleation and fabrication with rather limited synthetic control. Fabricating spatially periodic superstructure nanowires with accurately controllable space distribution of compositions and

https://doi.org/10.1021/acsnano.4c05205
ACS Nano 2024, 18, 18022−18035

electronic structures is still challenging and typically involves tedious synthesis methods, high preparation costs, and weak controllability, which may seriously hinder future applications.

Herein, we report on wafer-scale controllable growth of perovskite periodic heterojunction nanowire superlattices by an improved chemical vapor deposition (CVD) approach. This method is an effective synthesis approach that could overcome the poor controllability of the perovskite solid sources under high temperatures and produce a reasonable strategy to fabricate periodic perovskite nanowire superlattice arrays. Structural characterization demonstrates precisely periodic modulation of the composition in the heterostructure nanowires. At the same time, two different periodic intervals are observed ($\sqrt{3}$ μm and 1 μm) along the single periodic nanowire superlattice. Spatially resolved micro-photoluminescence (μ-PL) spectra and optical mapping images reveal that the heterostructure wires have periodically arranged heterojunctions with two emission bands at 415 and 692 nm, respectively. Moreover, high-performance photodetectors are systematically investigated based on these unique axial periodic $CsPbCl_3/CsPbI_3$ nanowire superlattices. Compared with single-component $CsPbCl_3$ nanowire photodetectors, the nanowire superlattice photodetector shows an expected superior performance, including a high I_{ON}/I_{OFF} ratio of 10^4, high responsivity of 49 A/W, and high specific detectivity of 1.51×10^{13} Jones. These results suggest that the periodic perovskite nanowire superlattices may have potential applications in high-integrated and multifunctional optoelectronic devices in the future.

RESULTS AND DISCUSSION

Figure 1a,b shows the top view and side view schematic drawing of the fabrication process and growth model for the $CsPbCl_3/CsPbI_3$ periodic perovskite nanowire superlattices on an annealed *M*-plane sapphire (see details in the Experimental Section), respectively. It is well known that *M*-plane sapphire α-Al_2O_3 $(10\bar{1}0)$ is thermodynamically unstable and forms periodic "line-shaped" grooves by annealing at high temperature.[72] First, a 2 in. *M*-plane sapphire wafer was periodically punched to create a periodic hole array (Figure 1a_1,a_2,b_1,b_2) for the nucleation sites of heterojunctions by the photolithographic technique. After that, this prefabricated *M*-plane substrate was annealed for 10 h at 1700 °C to form "line-shaped" grooves,[55,72−74] which was used for the horizontally guided growth of nanowires, as shown in Figure 1a_3. Second, tin catalyst nanoparticles were printed on the surface of the sapphire substrate (Figure 1a_4 and 1b_3), which was used for the growth of $CsPbCl_3/CsPbI_3$ periodic perovskite heterostructure nanowires utilizing a developed magnetic-pulling source-moving CVD approach (see the Experimental Section). More details of the growth processes are shown in Figure S1 (see the Supporting Information). Third, $CsPbCl_3$ nanowires were grown horizontally on the sapphire substrate through a vapor−liquid−solid (V−L−S) mechanism guided along the "line-shaped" grooves by a catalyst as plotted in Figure 1a_5,b_4. Due to the created periodic hole array along the grooves, $CsPbCl_3$ nanowires with periodic fracture defects were formed at the positions of the holes, which were precisely controlled and well matched with the position of the hole array as indicated in Figure 1b_4. These periodic artificial holes cause radial stress during the horizontally guided growth of nanowires, which results in periodic fracture defects at the positions of the holes. The scanning electron microscopy (SEM) and energy-dispersive X-ray spectroscopy (EDX) analyses of $CsPbCl_3$ nanowires with periodic fracture defects were performed, and the results are shown in Figures S2 and S3 (see the Supporting Information). As can be seen, 2D elemental maps and elemental profile line scans reveal that these horizontally guided nanowires show a uniform distribution of Cs, Pb, and Cl elements along the wires with composition fluctuation at the hole positions (Figure S2, see the Supporting Information). The EDX spectra from 10 positions of the wire are shown in Figure S3 (see the Supporting Information), and the corresponding atomic ratio of Cs, Pb, and Cl is close to (1:1:3), suggesting a pure $CsPbCl_3$ nanowire with periodic fracture defects on the wire. Fourth, when the sources were switched by a magnetic-pulling CVD system (see details in the Materials Preparation section), the Cl^- ions can be exchanged precisely by the I^- ions at the periodic fractured defects (Figures 1b_5 and S4, see the Supporting Information) and completely replaced and eventually formed the periodic $CsPbCl_3$−$CsPbI_3$ heterojunctions (Figure 1a_6,b_6). It is worth noting that the $CsPbI_3$ component was preferentially nucleated at the locations of the fractured defects (the positions of hole array) in the $CsPbCl_3$ nanowires, where the crystal binding energy in the formation of the nanowire is relatively lower.[64,75] Last, the horizontally guided $CsPbCl_3/CsPbI_3$ periodic nanowire superlattices were obtained on the *M*-plane sapphire, as shown in Figure 1a_6,b_6. This schematic diagram showing the proposed growth process indicates that the $CsPbI_3$ phase nucleated preferentially and grew on the positions of periodic fracture defects of $CsPbCl_3$ nanowires (rather than the *M*-sapphire substrate or the body of the $CsPbCl_3$ wire) to produce nanowire superlattices with periodic heterojunctions along the wires through a vapor−solid mechanism. Meanwhile, the optical photographs of wafer-scale sapphire substrates before and after the growth of $CsPbCl_3/CsPbI_3$ periodic heterostructure nanowires are shown in Figure S5, It is noted that the substrate has colored stripes after being punched by the lithography process, which may be caused by the light dispersion on a patterned sapphire substrate.

Figure 1c,d shows the top and side view SEM images of the *M*-plane sapphire with the $\sqrt{3}$ μm spacing periodic hole array, respectively, as indicated by the green dot array in Figure 1a_2. SEM images reveal that the hole array exhibits an upper and lower aperture of about 500 and 150 nm and a depth of about 350 nm (Figure 1c,d), respectively. Figure 1e,f exhibits low- and high-resolution SEM images of the sapphire after annealing, as indicated in Figure 1a_3 (purple dotted rectangle), from which hole arrays with "line-shaped" grooves are clearly exhibited. After that, the catalyst arrays are printed on the surface of the annealed *M*-plane sapphire substrates. The artificially constructed *M*-plane sapphire substrate with "line-shaped" grooves and hole array is a good candidate for the growth of horizontally guided perovskite heterojunction nanowires. Figure 1g,h shows low- and high-resolution SEM images of the as-grown periodic perovskite nanowire superlattice arrays grown on the annealed *M*-plane sapphire surfaces with grooves. In contrast, no aligned nanowires are observed for unannealed *M*-plane sapphire surfaces without grooves, indicating that the "line-shaped" grooves on the sapphire substrate play a key role in the alignment of nanowires. The as-fabricated $CsPbCl_3/CsPbI_3$ periodic heterostructure nanowires are self-aligned along the grooves with the $\pm 1\bar{2}10_{Al2O3}$

https://doi.org/10.1021/acsnano.4c05205
ACS Nano 2024, 18, 18022−18035

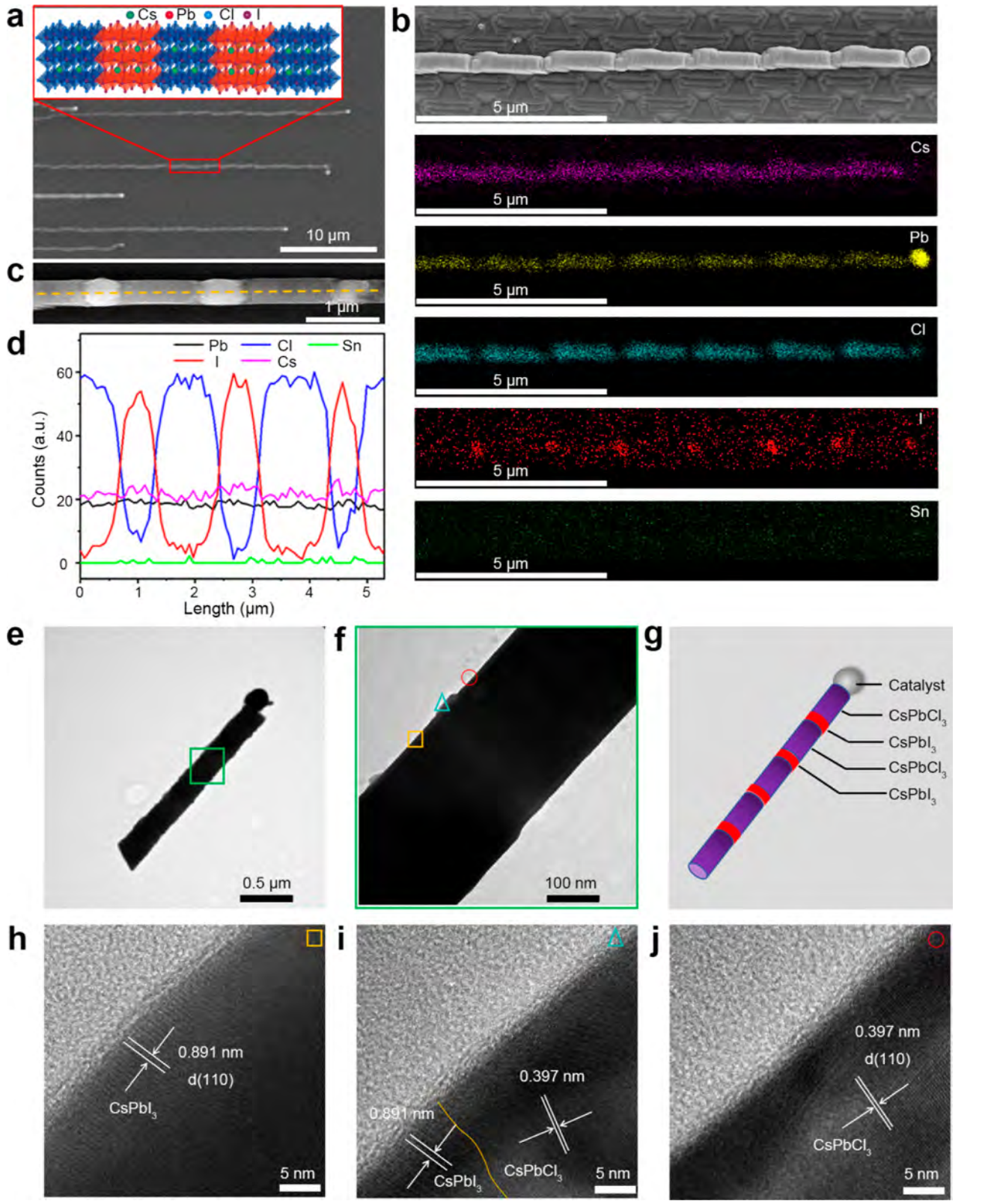

Figure 2. Compositional and structural characterization of a typical periodic nanowire superlattice. (a) Enlarged top view SEM image of some typical $CsPbCl_3/CsPbI_3$ periodic nanowire superlattices horizontally guided grown on a prefabricated *M*-plane sapphire substrate. Inset: schematic diagram of the atomic structure of $CsPbCl_3/CsPbI_3$ periodic nanowire superlattices. (b) SEM image and 2D EDX elemental mappings of a single periodic nanowire superlattice. (c,d) Typical HAADF-STEM image and elemental profile line scan of the nanowire [dotted line as shown in (c)]. (e,f) Low-resolution TEM images and corresponding structural schematic diagram (g) of a typical periodic superstructure nanowire. (h−j) HR-TEM images of three typical positions along a single periodic nanowire superlattice.

https://doi.org/10.1021/acsnano.4c05205
ACS Nano 2024, 18, 18022−18035

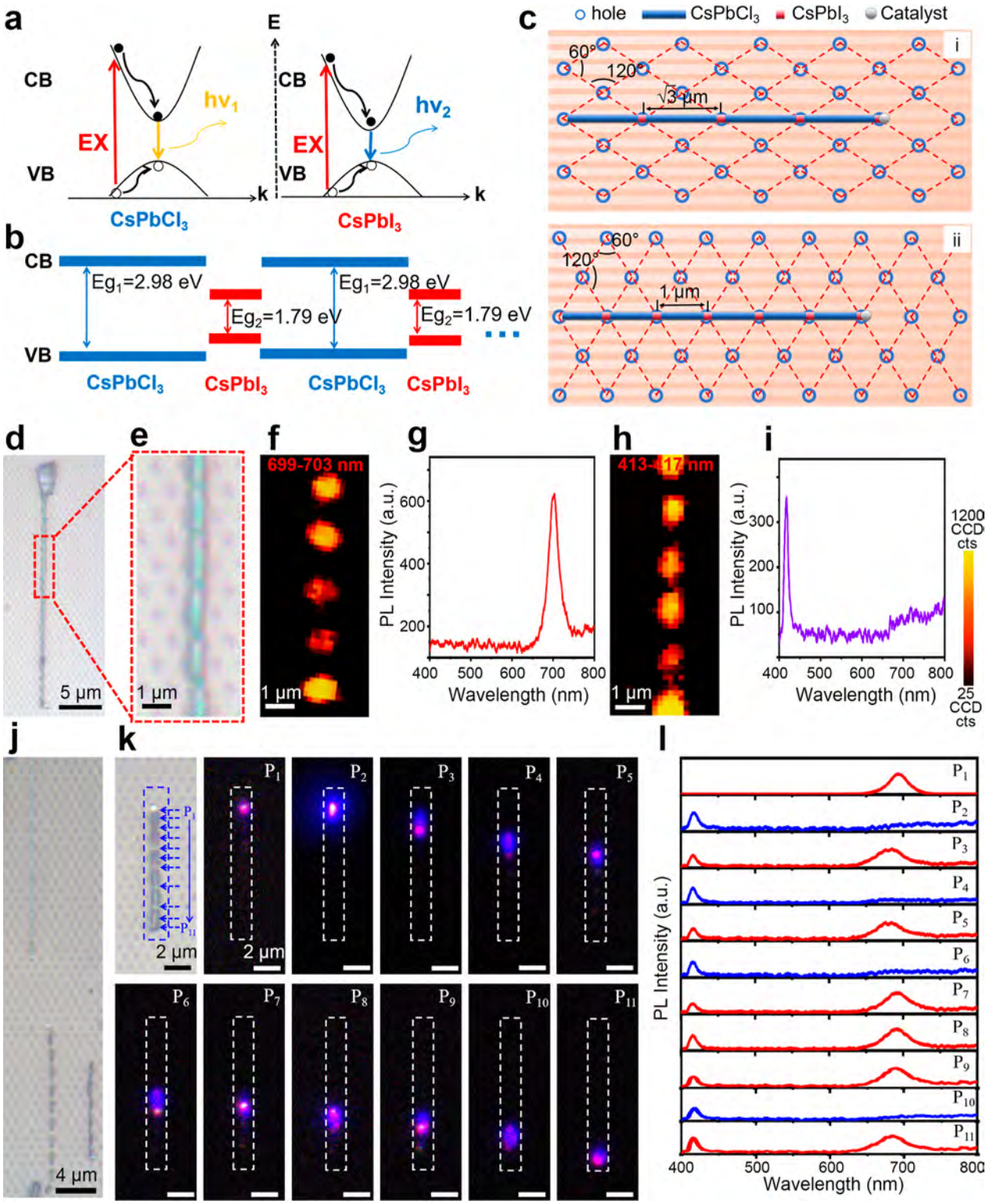

Figure 3. Room-temperature optical characterization of periodic perovskite nanowire superlattices. (a) Schematic illustration of the energy band diagrams of $CsPbCl_3$ and $CsPbI_3$ under light illumination. (b) Schematic diagram showing the energy band offsets at heterojunctions of $CsPbCl_3/CsPbI_3$ periodic perovskite nanowire superlattices. (c) Schematic drawing of nanowires with two different spacings [$\sqrt{3}$ μm type (i) and 1 μm type (ii)] between adjacent heterojunctions along "line-shaped" grooves. (d, e) Low- and high-resolution optical photographs of the nanowire superlattices on a *M*-plane sapphire. The enlarged section (e) of the optical image in (d) shows five periodic heterojunctions. (f–i) PL mapping and corresponding spectra of the selected periodic nanowire superlattices (as indicated in (e)). The scanning wavelength ranges are 699–703 and 413–417 nm, respectively. (j) Optical image of representative perovskite periodic nanowire superlattices. (k) Optical images and dark-field emission images (P_1–P_{11}) of a typical periodic perovskite nanowire superlattice under focused laser illumination. (l) Corresponding μ-PL spectra (P_1–P_{11}) as indicated in (k).

https://doi.org/10.1021/acsnano.4c05205
ACS Nano 2024, 18, 18022–18035

directions (Figure 1g). These nanowires have a length of 20−50 μm, a diameter ranging from 100 to 500 nm, and a heterojunction spacing of $\sqrt{3}$ μm, which are horizontally guided grown on the prefabricated *M*-plane sapphire substrate (pink rectangle, as indicated in Figure 1a$_6$).

Based on the precisely controlled nanowire superlattices, composition and structural characterizations were systematically performed in Figure 2. A close-up SEM image and a schematic atomic structure (inset image) of typical periodic $CsPbCl_3/CsPbI_3$ nanowire superlattices are shown in Figure 2a, respectively, in which two distinct regions ($CsPbCl_3$, blue region and $CsPbI_3$, red region in the inset image of Figure 2a) can be obtained clearly with different components. It is observed that these nanowires have periodic heterojunctions along a single wire. Moreover, a catalyst is located at the wire's tip, indicating a V−L−S growth mechanism of the nanowires. A high-resolution SEM image and two-dimensional (2D) elemental mappings for the five detected elements (Cs, Pb, Cl, I, and Sn) are shown in Figure 2b, suggesting a uniform distribution of the Cs and Pb elements along the wire. Meanwhile, Cl and I appear to be periodically changed and complementary to each other along the whole wire body. Figure 2c,d shows the high-angle annular dark-field scanning transmission electron microscopy (HAADF-STEM) image and line scans of elemental profiles along the length of a typical wire (dotted line, as indicated in 2c). The I and Cl concentrations show abrupt periodic and complementary trends along the length direction of the wire (red and blue lines in Figure 2d). The EDX spectra from six typical positions (points 1−6, as indicated in Figure S6, see the Supporting Information) show that Cs, Pb, Cl, and I are mainly present in the nanowire, and the atomic ratio of Cs, Pb, and (Cl or I) is close to 1:1:3 with negligible Sn in the wires. These elemental analyses, combined with the line scanning elemental profiles, confirm that these wires are indeed $CsPbCl_3/CsPbI_3$ heterostructure nanowires with periodic $CsPbCl_3$−$CsPbI_3$ crystal units along the entire wires and illustrate the formation of near-perfect abrupt heterointerfaces at the junctions.

Detailed microstructural properties and the crystallinity of the synthesized periodic $CsPbCl_3/CsPbI_3$ nanowire superlattices were investigated by transmission electron microscopy (TEM). Figure 2e shows a low-resolution TEM image of a representative $CsPbCl_3/CsPbI_3$ nanowire, which was picked out from the sapphire substrate by three-dimensional (3D) mechanical arms (details are shown in Figure S7, see the Supporting Information). Figure 2f shows the enlarged TEM image (indicted by a green square in Figure 2e) of the selected wire, indicating a uniform diameter of about 320 nm. Structural schematic diagram of a typical periodic superstructure nanowire is shown in Figure 2g, which exhibits the periodic structures along the axial direction and the catalyst on the tip of the nanowire. Figure 2h−j shows the high-resolution TEM (HR-TEM) images taken from three typical positions along a heterojunction of a $CsPbCl_3/CsPbI_3$ nanowire superlattice (see "□", "Δ", and "○" in Figure 2f), which exhibit a high-quality single-crystalline nanostructure without significant crystalline defects. The measured (110) lattice spacing in the orthorhombic phase $CsPbI_3$ region is 0.891 nm (Figure 2h). The 0.397 nm spacing in Figure 2j consisted of the (110) lattice spacing of orthorhombic $CsPbCl_3$.[74] Figure 2i clearly shows a well-defined heterointerface (shown with the orange line), where the $CsPbCl_3$ and $CsPbI_3$ parts maintain their respective single-crystalline structures. These results demonstrate that high-quality $CsPbCl_3/CsPbI_3$ periodic nanowire superlattices can be synthesized successfully with relatively abrupt interfaces.

It is worth noting that the *M*-plane sapphire with artificially prepared hole array and "line-shaped" grooves is key for constructing $CsPbCl_3/CsPbI_3$ periodic perovskite nanowire superlattices. In order to illustrate the important role of the hole array on the substrate, growths on Si/SiO_2 and *M*-plane sapphire substrates are compared. Figure S8 (see the Supporting Information) shows the SEM images and elemental investigations of the perovskite heterostructure wires grown on a Si/SiO_2 substrate. It can be seen that $CsPbCl_3/CsPbI_3$ perovskite nanowires with random heterojunctions are fabricated on the substrate. Optical characterization results of these perovskite $CsPbCl_3/CsPbI_3$ heterojunction nanowires are shown in Figure S9 (see the Supporting Information), which reveal that these wires have random multiple heterojunctions along the growth direction, in good agreement with the structural characterization results. Figure S10 (see the Supporting Information) shows the schematic of fabricated processes and SEM images of the $CsPbCl_3/CsPbI_3$ multi-heterojunction perovskite nanowire array grown on an annealed *M*-plane sapphire substrate, which has "line-shaped" grooves on the surface but without hole array. Optical investigations of the nanowire array (Figure S11, see the Supporting Information) further suggest that the wires are grown along the same directions with two emission peaks at the random heterojunctions. However, the locations of the heterojunctions cannot be controlled on the wires without the assistance of the "hole array" on the substrate. Moreover, the size of these nanoscale holes also plays a key role in the fabrication of the periodic nanowire superlattices. Figure S12 compares perovskite heterostructure nanowires grown on *M*-plane sapphire with different hole sizes. It can be seen that nanowires are grown randomly and disordered on the *M*-plane sapphire with bigger hole (d > 650 nm) size array (Figure S12a−d, see the Supporting Information), while the wires are horizontally guided growing along the "line-shaped" grooves on the *M*-plane sapphire with a smaller hole (d < 600 nm) size array (Figure S12e−h, see the Supporting Information). The growth direction of the disordered nanowires (Figure S12d, see the Supporting Information) is not along the "line-shaped" grooves as shown in Figure S13, which is different from the guided-grown nanowires in Figure S12h (see the Supporting Information). This is because the size of nanoscale holes is much bigger in Figure S12d than in Figure S12h (see the Supporting Information), so the catalysts will fall into the nearby holes (white dotted circle in insets, as indicated in Figure S13a,b, see the Supporting Information) next to the "line-shaped" grooves in the V−L−S growth process. Therefore, the nanowires grow randomly on the *M*-plane sapphire, as shown in Figures S12d and S13 (see the Supporting Information), respectively. Furthermore, *M*-plane sapphire substrates with a bigger hole array were annealed at various temperatures and annealing times and used to synthesize perovskite heterojunction nanowires (Figure S14, see the Supporting Information). Nanowires grown on these different sapphire substrates exhibit disordered growth directions, indicating that the annealing conditions have no obvious effect on the ordered growth of nanowires.

Figure 3a,b shows the schematic band diagrams for $CsPbCl_3$ (2.98 eV) and $CsPbI_3$ (1.79 eV) and the band alignments at the $CsPbCl_3/CsPbI_3$ periodic nanowire superlattices, respec-

https://doi.org/10.1021/acsnano.4c05205
ACS Nano 2024, 18, 18022−18035

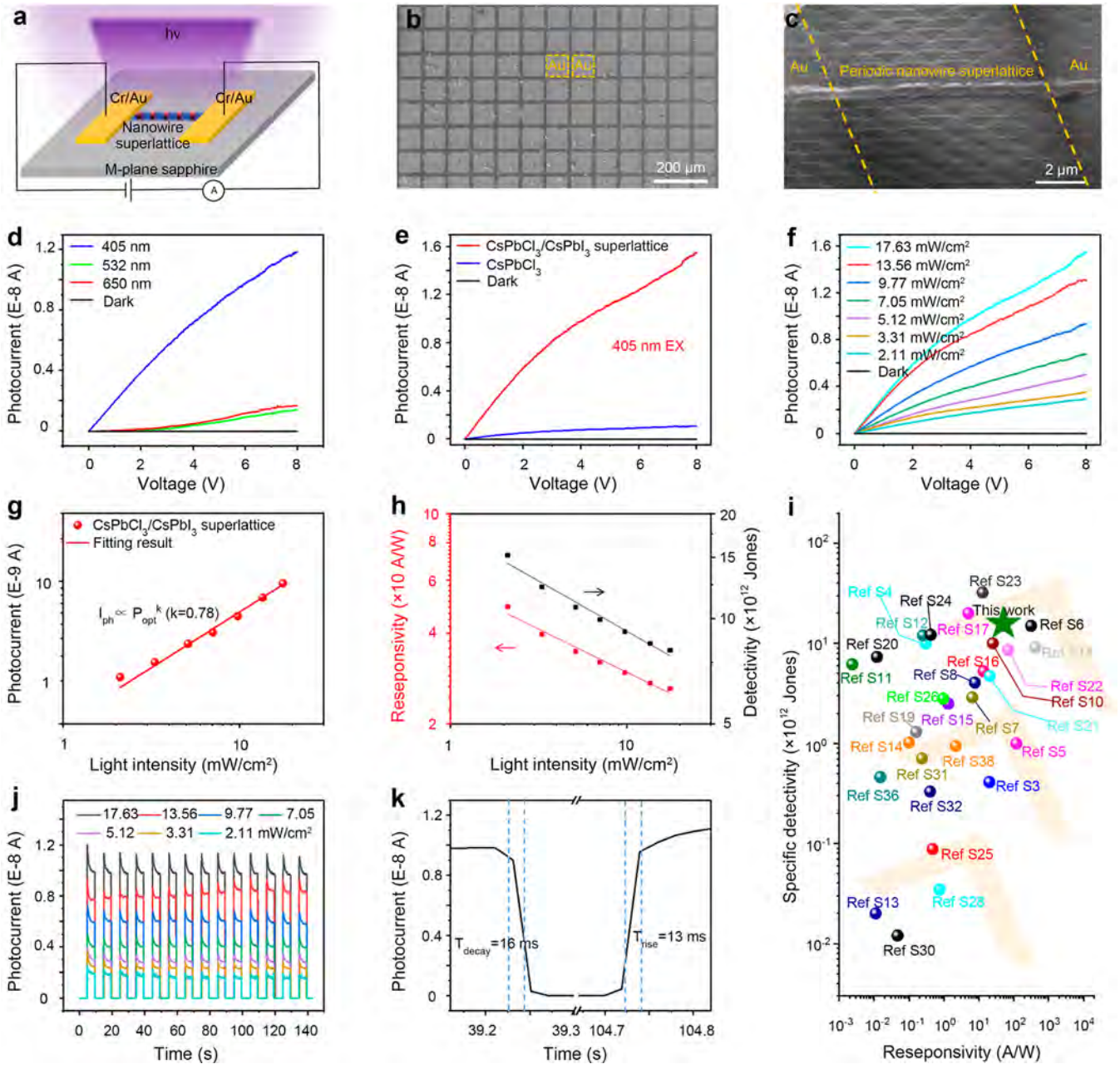

Figure 4. Optoelectronic characterization of $CsPbCl_3/CsPbI_3$ periodic nanowire superlattice photodetectors. (a) Schematic diagram of a photodetector based on perovskite nanowire superlattices. (b) SEM image of the device based on these nanowire superlattices. (c) Typical SEM image of a photodetector based on a single periodic perovskite superlattice. (d) *I*–*V* curves of photodetectors under illumination with lights at different wavelengths (17.63 mW/cm²) or in the dark. (e) *I*–*V* curves of devices based on the $CsPbCl_3/CsPbI_3$ periodic nanowire superlattice and pure $CsPbCl_3$ nanowire under 405 nm laser illumination and in the dark. (f) Pumping power-dependent *I*–*V* curves under 405 nm laser illumination. (g) Light intensity-dependent photocurrent at a voltage of 5 V. (h) Light intensity-dependent responsivity (red dots line) and detectivity (black dots line) of the device based on periodic nanowire superlattices under 405 nm illumination at a bias of 5 V. (i) Comparison of the responsivity and detectivity of the perovskite nanowire devices from this work with values reported in the literature. Detailed performance parameters are shown in Table S1 in the Supporting Information. (j) Pumping power density-dependent *I*–*T* measurements with 405 nm laser illumination under 5 V bias. (k) Response time (rise and decay time) of a nanowire superlattice photodetector under 405 nm laser illumination.

tively. As can be seen, $CsPbCl_3/CsPbI_3$ nanowire superlattices exhibit a type-II semiconductor band offset at the $CsPbCl_3$–$CsPbI_3$ interface. Figure 3c shows two schematic periodic nanowire superlattice models with various $CsPbCl_3$ segments (segment length: 1 μm and $\sqrt{3}$ μm). The two types of heterostructure nanowires are fabricated on different substrates, which have a corresponding heterojunction spacing of about 1 μm and $\sqrt{3}$ μm, respectively. The preparation of sapphire substrates with a hole spacing of 1 μm and $\sqrt{3}$ μm along the "line-shaped" grooves is illustrated in Figure S15 (see the Supporting Information). When the nanowires were growing through the hole array along the "line-shaped" grooves, two types of $CsPbCl_3/CsPbI_3$ nanowire superlattices with $CsPbCl_3$ segments of about 1 μm and $\sqrt{3}$ μm were

https://doi.org/10.1021/acsnano.4c05205
ACS Nano 2024, 18, 18022–18035

fabricated, as shown in Figure S16 (see the Supporting Information) and Figure 1, respectively. SEM images and EDX profiles (Figure S17, see the Supporting Information) of a typical $CsPbCl_3/CsPbI_3$ nanowire superlattice with $CsPbCl_3$ segments of 1 μm were also investigated. The results indicate periodic perovskite nanowire superlattices on the *M*-plane sapphire substrate, which agree well with the proposed growth mechanism in Figure 1. In addition, more details of the intermediate state of the growth process for $CsPbCl_3/CsPbI_3$ nanowire superlattices are shown in Figure S18 (see the Supporting Information), which show the SEM images and EDX profiles of a pure $CsPbCl_3$ nanowire with periodic defects (fracture defects with 1 μm spacing) along the wire length. After that, $CsPbI_3$ nucleation was formed at the periodic defects of the $CsPbCl_3$ wires to produce periodic $CsPbCl_3$–$CsPbI_3$ heterojunction interfaces at the positions of nanoscale holes.

To further probe the spatial structures of these wires, μ-PL spectra and 2D PL mapping of representative periodic perovskite nanowire superlattices with $\sqrt{3}$ μm $CsPbCl_3$ segments are performed using a confocal microscopic system (Figure S19, see the Supporting Information), and results are shown in Figure 3d–l. Figure 3d,e shows an optical photograph and an enlarged segment (red dotted square in part 3d) of a typical wire. These images clearly depict a "bamboo-like" structure with $CsPbI_3$ heterojunctions at the hole positions. 2D PL maps (Figure 3f,h) and their corresponding PL spectra (see Figure 3g,i) of the typical wire further demonstrate that two emission bands, blue (413–417 nm) and red (699–703 nm), appear periodically along a single nanowire. It is worth noting in the enlarged photograph that the five $CsPbCl_3/CsPbI_3$ heterojunctions are located at the same positions as the as-prepared nanoscale holes. This observation is in good agreement with the structural characterization results (Figure 2) and optical observations (Figure 3j). A series of μ-PL spectra and corresponding dark-field emission images were obtained from 11 representative positions along a single nanowire superlattice (P_1–P_{11} in Figure 3k). Dual-color emissions with peaks centered at 692 and 415 nm (Figure 3l) are shown at the heterojunctions (P_3, P_5, P_7, P_8, P_9, and P_{11}), which agree well with the reported bandgap of $CsPbCl_3$ (2.98 eV) and $CsPbI_3$ (1.79 eV), accordingly.[76−79] The two emission peaks appear at the $CsPbI_3$ segments because the laser spot is bigger than the $CsPbI_3$ size. On the other hand, a single emission peak centered at 415 nm is obtained from $CsPbCl_3$ segments (P_2, P_4, P_6, and P_{10}). It is worth noting that no obvious defect-state-related emission is identified across the entire wire, which indicates a high-quality $CsPbCl_3/CsPbI_3$ periodic heterostructure nanowire, in good agreement with the TEM observations in Figure 2h–j. Furthermore, the optical properties of the $CsPbCl_3/CsPbI_3$ perovskite nanowire superlattices with 1 μm periodic junction spacing are also shown in Figures S20 and S21 (see the Supporting Information). 2D PL mapping and PL spectra of the wires also indicate excellent periodic nanowire superlattices with abrupt heterojunctions. These unique periodic perovskite superlattices may offer an exciting material platform for multifunctional devices and circuits.

The above discussions clearly demonstrate the successful realization of $CsPbCl_3/CsPbI_3$ periodic perovskite nanowire superlattice arrays. To demonstrate their potential applications, photodetectors based on these perovskite superstructures were fabricated on an *M*-plane sapphire substrate, and their optoelectronic properties were systematically studied. Figure 4a shows a schematic diagram of a photodetector fabricated by using an individual $CsPbCl_3/CsPbI_3$ periodic nanowire superlattice. The corresponding SEM images of the device arrays are shown in Figure 4b, in which the Cr/Au (50 nm/80 nm) electrodes with a gap of 10 μm are thermally deposited on both ends of the wires. Figure 4c shows a close-up SEM image of a typical photodetector, in which periodic heterojunctions and hole arrays can be clearly observed. A photodetector based on a single $CsPbCl_3$ nanowire with the same size as the periodic superstructures (length = 11 μm and diameter = 380 nm) was also constructed and investigated for comparison, as shown in Figure S22 (see the Supporting Information).

The current–voltage (I_{ph}–V_{ds}) characteristics of the photodetectors based on periodic nanowire superlattices exposed to light of different wavelengths (P_{opt} = 17.63 mW/cm^2, λ = 405, 532, and 650 nm) ($I_{ph} = I_{light} - I_{dark}$) or under dark conditions are shown in Figure 4d. The conductance of the perovskite superstructures is very small in dark condition (only $\sim 10^{-12}$ A), while a high current of 1.18×10^{-8} A is recorded at an applied voltage of 8 V under a 405 nm laser at a power intensity of 17.63 mW/cm^2. The photocurrent increases dramatically by 4 orders of magnitude from 1.14×10^{-12} A to 1.18×10^{-8} A, 1.40×10^{-9} A, and 1.67×10^{-9} A when illuminated with different light (405, 532, and 650 nm) at a power intensity of P_{opt} = 17.63 mW/cm^2, which indicates a high sensitivity of the photodetectors. Figure 4e compares the results of the photocurrent photodetectors fabricated from $CsPbCl_3/CsPbI_3$ periodic nanowire superlattices and pure $CsPbCl_3$ nanowires in the dark and under 405 nm light illumination with a power density of 17.63 mW/cm^2. The photocurrent response of the photodetector based on the periodic nanowire superlattices (red line) is about 10 times higher than that based on the pure $CsPbCl_3$ nanowire (blue line). The power density dependence of the photoresponse of the photodetectors based on periodic nanowire superlattices under 405 nm laser illumination is shown in Figure 4f. As can be seen, the photocurrent of the photodetector increases gradually with the light power density and reaches the values $>10^{-8}$ A at a power density of 17.63 mW/cm^2. Compared with the dark current (10^{-12} A) and photocurrent of photodetectors based on pure $CsPbCl_3$ wires (1.11 nA, Figure S22, see the Supporting Information), the photocurrent increases by more than 4 orders and 1 order of magnitude, respectively. These results suggest that the photodetectors based on the periodic nanowire superlattices have a much larger photocurrent and, thus, a higher sensitivity. By fitting the relationship between I_{ph} and P_{opt} with the power law ($I_{ph} \propto P_{opt}^{k}$, k represents the correlation coefficient), k is evaluated as 0.78. Notably, this sublinear relationship between photocurrent and light intensity is observed in other nanowire-based photodetectors, which originates from the complex processes of electron–hole generation, trapping, and recombination in nanowires.[1,80]

The photoresponsivity (R) and detectivity (D^*) are two other important parameters to assess the performance of photodetectors. Figure 4h shows the light intensity dependent R and D^* of the photodetectors based on the periodic nanowire superlattices, which can be calculated by the equations as follows

https://doi.org/10.1021/acsnano.4c05205
ACS Nano 2024, 18, 18022–18035

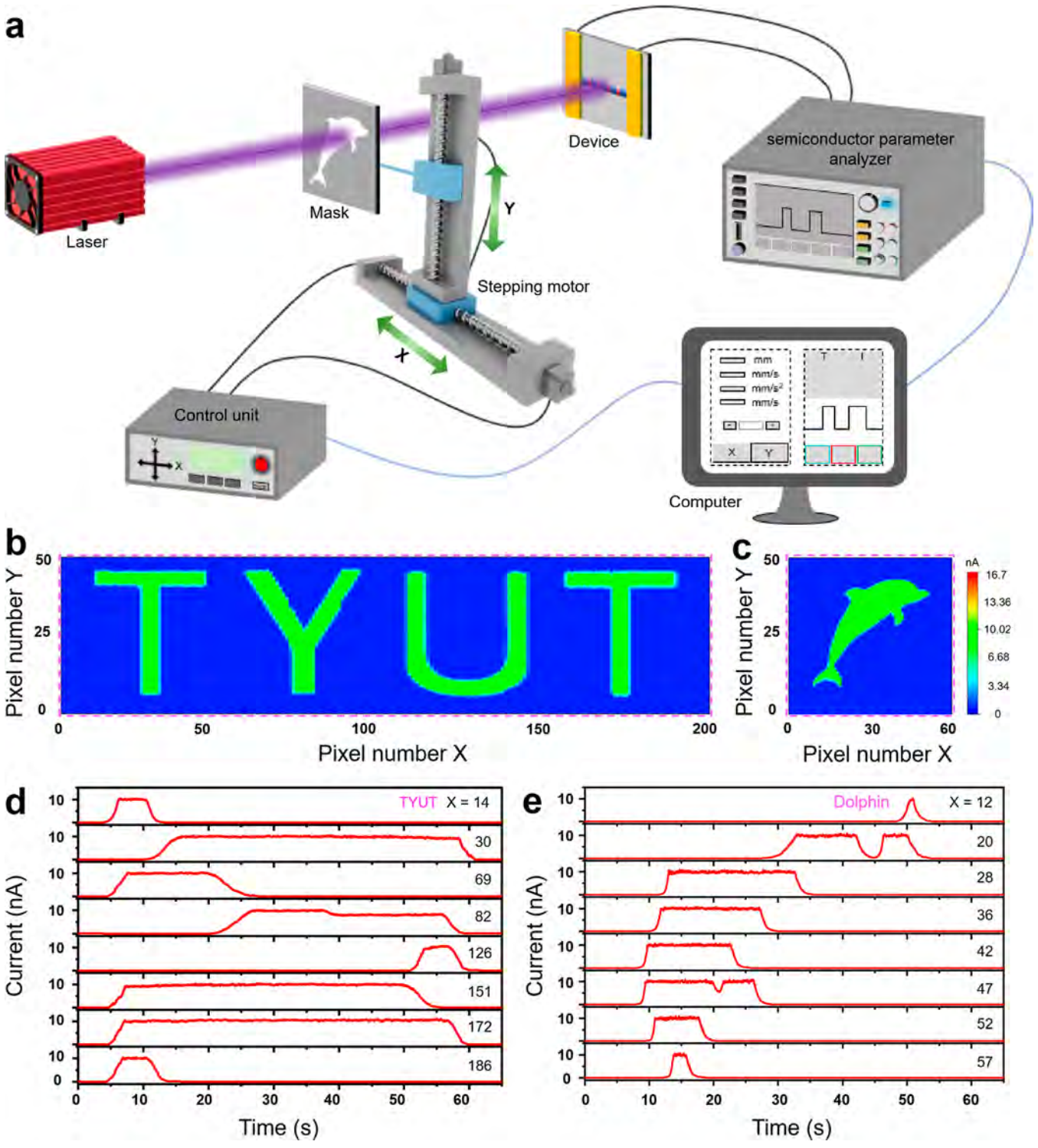

Figure 5. Image sensing application of the $CsPbCl_3/CsPbI_3$ periodic nanowire superlattices. (a) Schematic diagram of the photodetector imaging scanning system. (b,c) Corresponding two-dimensional photocurrent mapping of the images of "TYUT" and "Dolphin" under 405 nm laser illumination, respectively. Time-dependent current curves of "TYUT" (d) and "Dolphin" (e) under 405 nm laser scans along the *Y* direction with different *X* pixel points. The numbers on the right side denote the pixel sequences in the *X* direction.

$$R = \frac{I_{ph}}{P_{opt}A} \quad (1)$$

$$D^* = R\sqrt{\frac{A}{2eI_{dark}}} \quad (2)$$

where I_{ph} is the difference between the photocurrent and dark current, P_{opt} = 2.11 mW/cm^2 is the incident light power density illuminated at the periodic superstructures, A is an effective irradiated area on the device, and e is the electronic charge. Both R and D^* increase dramatically with a decrease in the light intensity. The periodic photodetector based on the nanowire superlattices shows a responsivity of about 49 A/W.

https://doi.org/10.1021/acsnano.4c05205
ACS Nano 2024, 18, 18022−18035

At the same time, the corresponding D^* is about 1.51×10^{13} Jones under 405 nm laser illumination with a light intensity of 2.11 mW/cm^2. Impressively, R and D^* values of the photodetectors based on periodic nanowire superlattices are much higher than that based on pure $CsPbCl_3$ wires (1.89 A/W and 3.98×10^{11} Jones). The performances of photodetectors based on most perovskite structures reported to date are shown in Figure 4i and Table S1 (see the Supporting Information).

The external quantum efficiency (EQE), which is the number of electron−hole pairs produced by one absorbed photon,[81] is a critical parameter for photodetectors and can be expressed as

$$\mathrm{EQE} = \frac{hcR}{e\lambda} \tag{3}$$

Thus, for the obtained R of 49 A/W, the corresponding calculated EQE is 1.5×10^4% for photodetectors based on the periodic superstructure, and the light intensity-dependent EQE characteristics of the photodetectors based on the periodic nanowire superlattices is shown in Figure S23. These measured values for the nanowire superlattices-based devices are much higher than those for the $CsPbCl_3$-based photodetector (1.89 A/W and 5.78×10^2%), as well as pure $CsPbCl_3$ photodetectors reported in the literature studies.[82,83] The time response of a photodetector based on the periodic nanowire superlattices with different light power intensities is shown in Figure 4j, which is investigated by periodically turning a 405 nm laser on and off under 5 V bias. The detector exhibits a high I_{ON}/I_{OFF} ratio (10^4), good stability, and reproducibility with rise and decay times of about 13 and 16 ms (Figure 4k), respectively, which are faster than those of the pure $CsPbCl_3$ device (30 and 33 ms) in this work (Figure S23, see the Supporting Information) and those reported from previous studies.[84,85]

According to the above results, all performance parameters for photodetectors based on our $CsPbCl_3/CsPbI_3$ periodic nanowire superlattices are superior to those of pure $CsPbCl_3$ nanowires. Moreover, photodetectors made from periodic nanowire superlattices also have a much broader light wavelength response in comparison to those made from pure $CsPbCl_3$. When a photodetector is excited by photons with energy higher than the bandgap, the photogenerated carriers will be directly transferred to form a photocurrent under external bias. Thus, a detector based on $CsPbCl_3/CsPbI_3$ nanowire superlattices not only produces photogenerated current when the photon energy E_{ph} is higher than the bandgap of $CsPbCl_3$ (>2.98 eV) but also have a photoresponse when the photon energy is lower than $CsPbCl_3$ but higher than $CsPbI_3$ ($1.79 < E_{ph} < 2.98$ eV) (Figure 4d). On the other hand, under illumination with photon energy higher than the $CsPbCl_3$ bandgap, the radiative electron−hole pair recombination in the device unless photon-generated carriers with energy close to the bandgap energy are emitted. This loss of radiative energy will directly lead to the low photoelectric detection efficiency of the device (Figure S22f, Supporting Information). As illustrated in Figure S24 (see the Supporting Information), the radiative photon energy from $CsPbCl_3$ is higher than the bandgap of $CsPbI_3$ and hence can be reabsorbed by $CsPbI_3$ on both sides and induces additional photocarriers. Consequently, the radiative energy loss is reduced during the light transmission process. Due to the multiple heterojunction interfaces along the axial direction of $CsPbCl_3/CsPbI_3$ periodic nanowire superlattices, this intermediately radiative reabsorption process (interenergy-transfer process) is greatly magnified. This interenergy-transfer process plays a key role for the high-performance photodetectors. It leads to the observed much enhanced photocurrent and responsivity in detectors based on the periodic nanowire superlattices compared to the pure $CsPbCl_3$ wires. Therefore, it is worth pointing out that such periodic nanowire superlattices are crucial for the improvement of photoelectronic properties of perovskite materials to extend their potential applications in optoelectronic devices.

In consideration of the high photosensitivity in the visible light region, the $CsPbCl_3/CsPbI_3$ periodic nanowire superlattice photodetectors hold good potential for image sensing applications. The schematic diagram of imaging principle is illustrated in Figure 5a. The shaped hollowed mask was placed between the light source (a 405 nm laser beam) and the device, and then the light beam could pass through the hollowed-out pattern and shed on the periodic nanowire superlattice photodetector. The image mask was moved and controlled by a two-dimensional ($X-Y$) step-motor platform in which the spatially resolved real-time response of the devices was recorded by a computer connected with a semiconductor analyzer. At last, high-resolution spatial images of both "TYUT" and "Dolphin" are being imaged as shown in Figure 5b,c. At different X pixel points, the 405 nm laser scans along the Y direction of the mask and the time-dependent photocurrent curves of the "TYUT" and "Dolphin" are displayed in Figure 5d,e, respectively. These impressive results demonstrate promising imaging applications of $CsPbCl_3/CsPbI_3$ periodic nanowire superlattice photodetectors.

CONCLUSIONS

In summary, a feasible synthesis approach is presented for the site-controlled growth of $CsPbCl_3/CsPbI_3$ periodic perovskite nanowire superlattices based on the combination of horizontally guided vapor−liquid−solid growth via a modified magnetic-pulling source-moving CVD method. Structural characterization clearly reveals that the as-grown perovskite nanowires have periodic $CsPbCl_3-CsPbI_3$ heterojunctions along a single wire with abrupt interfaces. 2D PL mapping and optical spectra along the nanowires further indicate periodic dual-wavelength emissions of 415 and 692 nm at every heterojunction, suggesting that these emission bands are spatially separated periodically along a single perovskite nanowire. Moreover, photodetectors based on these unique periodic superstructures show superior detection performance over the traditional pure $CsPbCl_3$ photodetectors, including a high I_{ON}/I_{OFF} ratio (10^4) and high responsivity (49 A/W), as well as high detectivity (1.51×10^{13} Jones). Ultimately, a high-resolution visible image sensor based on the $CsPbCl_3-CsPbI_3$ periodic nanowire superlattice photodetector as a single pixel has been demonstrated to identify its good imaging capability. Additionally, this proposed approach is not limited to the $CsPbCl_3/CsPbI_3$ system; in principle, different periodic nanowire superlattices can be synthesized by changing the compositions. Forming such horizontally aligned periodic perovskite superstructures with well-defined artificial heterojunctions and impressive features can provide exciting opportunities for creating a scalable fabrication of high-performance electronic and optoelectronic devices.

https://doi.org/10.1021/acsnano.4c05205
ACS Nano 2024, 18, 18022−18035

EXPERIMENTAL SECTION

Substrate Preparation. Si/SiO_2 substrates were cleaned by an ultrasonic bath in acetone, isopropyl alcohol, and distilled H_2O for 20 min, sequentially, and then cut into square pieces (2 cm × 1 cm) for use. 2 in. *M*-plane sapphire wafers were washed by an ultrasonic machine for 10 min in acetone, isopropyl alcohol, and distilled H_2O and blown dry by nitrogen. After that, hole arrays on the *M*-plane sapphire were obtained via the photolithography process. Before being annealed, the *M*-plane sapphire substrates were cleaned in acetone and isopropyl alcohol for 10 min. Then, the substrates were annealed in a high-temperature furnace (KRX-17B) at 1700 °C for 10 h. Last, the furnace was cooled, and the *M*-plane sapphire with "line-shaped" grooves and hole array was obtained.

Materials Preparation. Periodic perovskite nanowire superlattices were grown via a magnetic-pulling source-moving CVD strategy. A horizontal furnace (OTF-1200X) with a quartz tube (inner diameter: 45 mm and length: 180 cm) was used to grow the materials. Two quartz boats with $PbCl_2$/CsCl and PbI_2/CsI (Alfa Aesar, 99.99%, mole ratio = 1:2) powder separated by two quartz rods were placed in the center and upstream of the heating zone, respectively. The *M*-plane sapphire (2 in., thickness 430 μm) was placed at the deposition area to collect the products. Tin catalyst arrays were printed on the surface of the sapphire substrate by a mask. Before the growth, N_2 gas (150 sccm) was continually pumped into the quartz tube to remove residual oxygen. Then, N_2 gas flow (60 sccm) and H_2 gas flow (10 sccm) were introduced into the chamber, and the pressure was controlled at 5 Torr during the entire experiment. The temperature of the furnace was controlled, as shown in Figure S1 (see the Supporting Information). It is important that the right zone (Zone 2) was first ramped up to 380 °C at a rate of 25 °C/min before growth, in which the sapphire substrates were located. Then, the temperature in the left zone (Zone 1) was ramped up to 470 °C at a rate of 25 °C/min. After 60 min, the temperature of the two zones was reduced to 420 and 320 °C at a rate of 10 °C/min for the nucleation and growth of $CsPbI_3$. At this time, changing the source of the drug, specifically, the second quartz boat with PbI_2/CsI powder was pushed to the center of the left zone at a constant speed (20 cm/min) by a stepper motor, and the first quartz boat with $PbCl_2$/CsCl was pushed out of the heating zone. The temperature of two zone was maintained at 420 and 320 °C for 60 min, respectively. And then, the furnace was cooled down naturally. Notably, the growth temperature of $CsPbCl_3$ is a little higher than that of $CsPbI_3$, so thermal degradation of $CsPbCl_3$ is avoided during the growth of $CsPbI_3$ nanowires.

Materials Characterization. The morphologies of prefabricated *M*-plane sapphire substrate and perovskite structures were investigated via SEM (Hitachi SU-8010, Japan) with energy-dispersive EDX capability at an accelerating voltage of 6.0 kV and TEM (JEM-F200). The nanowires were transferred from the primary substrate to copper grids by 3D mechanical arms with homemade fiber probes, as schematically shown in Figure S7 (see the Supporting Information). Optical characteristics were studied with a confocal optical system. PL spectra were recorded by an Ocean Optics Spectrometer (MayaPro2000) with laser beams (375 and 488 nm) focused to 1.5 μm by a microscope (Nikon, × 100) and locally excited the heterostructures. In particular, in order to avoid the effect of high energy photons (375 nm) on the optical characterization of $CsPbI_3$, the red emission of optical mapping was performed by a 488 nm laser, and the blue emission of optical mapping was performed with a 375 nm laser.

Device Fabrication and Characterization. Cr/Au (50 nm/80 nm) layers were defined as source and drain-patterned electrodes on nanowire photodetectors by a thermal evaporation process with a shadow mask (a channel length of 10 μm). Device measurements of these $CsPbCl_3/CsPbI_3$ periodic nanowire superlattices and pure $CsPbCl_3$ nanowire-based detectors were performed on the probe station with a semiconductor parameter analyzer system (Keithley 2450). The photocurrent was obtained when the device operated under illumination (405, 532, and 650 nm). The current−voltage ($I_{ph}-V_{ds}$) characteristics sweep from 0 to 8 V under 405 nm illumination. The current−time ($I_{ph}-T$) characteristics response at 10 s intervals under 405 nm illumination when V_{ds} = 5 V. The illumination power density was adjusted by adding attenuating lenses (OMMB-NDFC5020), and the light power density was calibrated by a power meter (CNI-Laser-TP100). The movement of the image pattern mask is controlled by a stepper motor (Zolix-SC300).

ASSOCIATED CONTENT

Supporting Information

The Supporting Information is available free of charge at https://pubs.acs.org/doi/10.1021/acsnano.4c05205.

CVD setup, SEM image, EDX spectra, and optical photographs of the periodic heterostructure nanowires; comparison results of the periodic heterostructure nanowires with different hole sizes; schematic diagram of the confocal microscopy system; optoelectronic characterization of a typical $CsPbCl_3$ nanowire; energy-transfer process at the heterointerface; and synthesis process of photodetectors based on perovskite nanomaterials (PDF)

AUTHOR INFORMATION

Corresponding Authors

Pengfei Guo − *College of Electronic Information and Optical Engineering, Taiyuan University of Technology, Taiyuan 030024, China;* orcid.org/0000-0002-4785-0753; Email: guopengfei2010@126.com

Liantuan Xiao − *College of Electronic Information and Optical Engineering, Taiyuan University of Technology, Taiyuan 030024, China;* orcid.org/0000-0003-2690-6460; Email: xlt@sxu.edu.cn

Xidong Duan − *College of Chemistry and Chemical Engineering, Hunan University, Changsha 410082, China;* orcid.org/0000-0002-4951-901X; Email: xidongduan@hnu.edu.cn

Authors

Qihang Lv − *College of Electronic Information and Optical Engineering, Taiyuan University of Technology, Taiyuan 030024, China; College of Chemistry and Chemical Engineering, Hunan University, Changsha 410082, China*

Xia Shen − *College of Electronic Information and Optical Engineering, Taiyuan University of Technology, Taiyuan 030024, China*

Xuyang Li − *College of Electronic Information and Optical Engineering, Taiyuan University of Technology, Taiyuan 030024, China*

You Meng − *Department of Materials Science and Engineering, City University of Hong Kong, Kowloon, Hong Kong 999077, China*

Kin Man Yu − *Department of Physics, City University of Hong Kong, Kowloon, Hong Kong 999077, China;* orcid.org/0000-0003-1350-9642

Johnny C. Ho − *Department of Materials Science and Engineering, City University of Hong Kong, Kowloon, Hong Kong 999077, China;* orcid.org/0000-0003-3000-8794

Xiangfeng Duan − *Department of Chemistry and Biochemistry, University of California, Los Angeles, California 90095, United States;* orcid.org/0000-0002-4321-6288

Complete contact information is available at: https://pubs.acs.org/10.1021/acsnano.4c05205

https://doi.org/10.1021/acsnano.4c05205
ACS Nano 2024, 18, 18022−18035

Author Contributions

[#]Q.L., X.S., and X.L. contributed equally to this work.

Notes

The authors declare no competing financial interest.

ACKNOWLEDGMENTS

The authors are grateful to the National Natural Science Foundation of China (no. 52373246), the National Key Research and Development Program of China (no. 2022YFA1404201), the Shanxi Basic Research Program Project (no. 20210302123128), and a fellowship award from the Research Grants Council of the Hong Kong Special Administrative Region, China (CityU RFS2021-1S04), for financial support.

REFERENCES

(1) Meng, Y.; Lan, C.; Li, F.; Yip, S.; Wei, R.; Kang, X.; Bu, X.; Dong, R.; Zhang, H.; Ho, J. C. Direct Vapor-Liquid-Solid Synthesis of All-Inorganic Perovskite Nanowires for High-Performance Electronics and Optoelectronics. *ACS Nano* **2019**, *13* (5), 6060−6070.

(2) Li, X.; Meng, Y.; Li, W.; Zhang, J.; Dang, C.; Wang, H.; Hung, S. W.; Fan, R.; Chen, F. R.; Zhao, S.; Ho, J. C.; Lu, Y. Multislip-enabled morphing of all-inorganic perovskites. *Nat. Mater.* **2023**, *22* (10), 1175−1181.

(3) Schlaus, A. P.; Spencer, M. S.; Miyata, K.; Liu, F.; Wang, X.; Datta, I.; Lipson, M.; Pan, A.; Zhu, X. Y. How lasing happens in $CsPbBr_3$ perovskite nanowires. *Nat. Commun.* **2019**, *10* (1), 265.

(4) Waleed, A.; Tavakoli, M. M.; Gu, L.; Hussain, S.; Zhang, D.; Poddar, S.; Wang, Z.; Zhang, R.; Fan, Z. All Inorganic Cesium Lead Iodide Perovskite Nanowires with Stabilized Cubic Phase at Room Temperature and Nanowire Array-Based Photodetectors. *Nano Lett.* **2017**, *17* (8), 4951−4957.

(5) Oksenberg, E.; Merdasa, A.; Houben, L.; Kaplan-Ashiri, I.; Rothman, A.; Scheblykin, I. G.; Unger, E. L.; Joselevich, E. Large lattice distortions and size-dependent bandgap modulation in epitaxial halide perovskite nanowires. *Nat. Commun.* **2020**, *11* (1), 489.

(6) Ning, C. Z.; Dou, L.; Yang, P. Bandgap engineering in semiconductor alloy nanomaterials with widely tunable compositions. *Nat. Rev. Mater.* **2017**, *2* (12), 17070.

(7) Zhang, Y.; Parsonnet, E.; Fernandez, A.; Griffin, S. M.; Huyan, H.; Lin, C. K.; Lei, T.; Jin, J.; Barnard, E. S.; Raja, A.; Behera, P.; Pan, X.; Ramesh, R.; Yang, P. Ferroelectricity in a semiconducting all-inorganic halide perovskite. *Sci. Adv.* **2022**, *8* (6), No. eabj5881.

(8) Gao, Y.; Zhao, L.; Shang, Q.; Zhong, Y.; Liu, Z.; Chen, J.; Zhang, Z.; Shi, J.; Du, W.; Zhang, Y.; Chen, S.; Gao, P.; Liu, X.; Wang, X.; Zhang, Q. Ultrathin $CsPbX_3$ Nanowire Arrays with Strong Emission Anisotropy. *Adv. Mater.* **2018**, *30* (31), 1801805.

(9) Eaton, S. W.; Lai, M.; Gibson, N. A.; Wong, A. B.; Dou, L.; Ma, J.; Wang, L. W.; Leone, S. R.; Yang, P. Lasing in robust cesium lead halide perovskite nanowires. *Proc. Natl. Acad. Sci. U.S.A.* **2016**, *113* (8), 1993−1998.

(10) Meng, Y.; Zhang, Y.; Lai, Z.; Wang, W.; Wang, W.; Li, Y.; Li, D.; Xie, P.; Yin, D.; Chen, D.; Liu, C.; Yip, S.; Ho, J. C. Au-Seeded $CsPbI_3$ Nanowire Optoelectronics via Exothermic Nucleation. *Nano Lett.* **2023**, *23* (3), 812−819.

(11) Oksenberg, E.; Sanders, E.; Popovitz-Biro, R.; Houben, L.; Joselevich, E. Surface-Guided $CsPbBr_3$ Perovskite Nanowires on Flat and Faceted Sapphire with Size-Dependent Photoluminescence and Fast Photoconductive Response. *Nano Lett.* **2018**, *18* (1), 424−433.

(12) Lou, Y.; Zhang, S.; Gu, Z.; Wang, N.; Wang, S.; Zhang, Y.; Song, Y. Perovskite single crystals: Dimensional control, optoelectronic properties, and applications. *Mater. Today* **2023**, *62*, 225−250.

(13) Gu, Z.; Zhao, Y.; Zhang, Y.; Huang, Z.; Zhou, Z.; Wang, K.; Li, L.; Zhao, Y. S.; Xu, Q.; Song, Y. Ion Aggregation-Induced Crystallization Strategy for Printing Morphology-Controllable Perovskite Single-Crystal Arrays and Integrated Devices. *Chem. Mater.* **2023**, *35* (13), 5127−5134.

(14) Zhang, D.; Yang, Y.; Bekenstein, Y.; Yu, Y.; Gibson, N. A.; Wong, A. B.; Eaton, S. W.; Kornienko, N.; Kong, Q.; Lai, M.; Alivisatos, A. P.; Leone, S. R.; Yang, P. Synthesis of Composition Tunable and Highly Luminescent Cesium Lead Halide Nanowires through Anion-Exchange Reactions. *J. Am. Chem. Soc.* **2016**, *138* (23), 7236−7239.

(15) Fu, Y.; Zhu, H.; Stoumpos, C. C.; Ding, Q.; Wang, J.; Kanatzidis, M. G.; Zhu, X.; Jin, S. Broad Wavelength Tunable Robust Lasing from Single-Crystal Nanowires of Cesium Lead Halide Perovskites ($CsPbX_3$, X = Cl, Br, I). *ACS Nano* **2016**, *10* (8), 7963−7972.

(16) Zhou, H.; Yuan, S.; Wang, X.; Xu, T.; Wang, X.; Li, H.; Zheng, W.; Fan, P.; Li, Y.; Sun, L.; Pan, A. Vapor Growth and Tunable Lasing of Band Gap Engineered Cesium Lead Halide Perovskite Micro/Nanorods with Triangular Cross Section. *ACS Nano* **2017**, *11* (2), 1189−1195.

(17) Zhu, H.; Fu, Y.; Meng, F.; Wu, X.; Gong, Z.; Ding, Q.; Gustafsson, M. V.; Trinh, M. T.; Jin, S.; Zhu, X. Y. Lead halide perovskite nanowire lasers with low lasing thresholds and high quality factors. *Nat. Mater.* **2015**, *14* (6), 636−642.

(18) Liu, P.; He, X.; Ren, J.; Liao, Q.; Yao, J.; Fu, H. Organic-Inorganic Hybrid Perovskite Nanowire Laser Arrays. *ACS Nano* **2017**, *11* (6), 5766−5773.

(19) Protesescu, L.; Yakunin, S.; Bodnarchuk, M. I.; Krieg, F.; Caputo, R.; Hendon, C. H.; Yang, R. X.; Walsh, A.; Kovalenko, M. V. Nanocrystals of Cesium Lead Halide Perovskites ($CsPbX_3$, X = Cl, Br, and I): Novel Optoelectronic Materials Showing Bright Emission with Wide Color Gamut. *Nano Lett.* **2015**, *15* (6), 3692−3696.

(20) Lin, X.; Chen, L.; He, C.; Wang, Y.; Li, X.; Dang, W.; He, K.; Huangfu, Y.; Wu, D.; Zhao, B.; Li, B.; Li, J.; Duan, X. Vapor Phase Growth of Centimeter-Sized Band Gap Engineered Cesium Lead Halide Perovskite Single-Crystal Thin Films with Color-tunable Stimulated Emission. *Adv. Funct. Mater.* **2023**, *33* (1), 2210278.

(21) Fu, Y.; Yuan, M.; Zhao, Y.; Dong, M.; Guo, Y.; Wang, K.; Jin, C.; Feng, J.; Wu, Y.; Jiang, L. Gradient Bandgap-Tunable Perovskite Microwire Arrays toward Flexible Color-Cognitive Devices. *Adv. Funct. Mater.* **2023**, *33* (11), 2214094.

(22) Islam, M. J.; Yuyama, K. i.; Takahashi, K.; Nakamura, T.; Konishi, K.; Biju, V. Mixed-halide perovskite synthesis by chemical reaction and crystal nucleation under an optical potential. *NPG Asia Mater.* **2019**, *11* (1), 31.

(23) Tian, T.; Yang, M.; Fang, Y.; Zhang, S.; Chen, Y.; Wang, L.; Wu, W. Q. Large-area waterproof and durable perovskite luminescent textiles. *Nat. Commun.* **2023**, *14* (1), 234.

(24) Su, R.; Fieramosca, A.; Zhang, Q.; Nguyen, H. S.; Deleporte, E.; Chen, Z.; Sanvitto, D.; Liew, T. C. H.; Xiong, Q. Perovskite semiconductors for room-temperature exciton-polaritonics. *Nat. Mater.* **2021**, *20* (10), 1315−1324.

(25) Fu, Y.; Zhu, H.; Chen, J.; Hautzinger, M. P.; Zhu, X. Y.; Jin, S. Metal halide perovskite nanostructures for optoelectronic applications and the study of physical properties. *Nat. Rev. Mater.* **2019**, *4* (3), 169−188.

(26) Cen, G.; Xia, Y.; Zhao, C.; Fu, Y.; An, Y.; Yuan, Y.; Shi, T.; Mai, W. Precise Phase Control of Large-Scale Inorganic Perovskites via Vapor-Phase Anion-Exchange Strategy. *Small* **2020**, *16* (52), 2005226.

(27) Qi, X.; Zhang, Y.; Ou, Q.; Ha, S. T.; Qiu, C.-W.; Zhang, H.; Cheng, Y.-B.; Xiong, Q.; Bao, Q. Photonics and Optoelectronics of 2D Metal-Halide Perovskites. *Small* **2018**, *14* (31), 1800682.

(28) Singh, A.; Yuan, B.; Rahman, M. H.; Yang, H.; De, A.; Park, J. Y.; Zhang, S.; Huang, L.; Mannodi-Kanakkithodi, A.; Pennycook, T. J.; Dou, L. Two-Dimensional Halide Pb-Perovskite-Double Perovskite Epitaxial Heterostructures. *J. Am. Chem. Soc.* **2023**, *145* (36), 19885−19893.

(29) Pan, D.; Fu, Y.; Spitha, N.; Zhao, Y.; Roy, C. R.; Morrow, D. J.; Kohler, D. D.; Wright, J. C.; Jin, S. Deterministic fabrication of arbitrary vertical heterostructures of two-dimensional Ruddlesden-Popper halide perovskites. *Nat. Nanotechnol.* **2021**, *16* (2), 159−165.

https://doi.org/10.1021/acsnano.4c05205
ACS Nano 2024, 18, 18022−18035

(30) Shi, E.; Yuan, B.; Shiring, S. B.; Gao, Y.; Akriti; Guo, Y.; Su, C.; Lai, M.; Yang, P.; Kong, J.; Savoie, B. M.; Yu, Y.; Dou, L. Two-dimensional halide perovskite lateral epitaxial heterostructures. *Nature* **2020**, *580* (7805), 614−620.
(31) Tian, W.; Leng, J.; Zhao, C.; Jin, S. Long-Distance Charge Carrier Funneling in Perovskite Nanowires Enabled by Built-in Halide Gradient. *J. Am. Chem. Soc.* **2017**, *139* (2), 579−582.
(32) Wang, Y.; Chen, Z.; Deschler, F.; Sun, X.; Lu, T. M.; Wertz, E. A.; Hu, J. M.; Shi, J. Epitaxial Halide Perovskite Lateral Double Heterostructure. *ACS Nano* **2017**, *11* (3), 3355−3364.
(33) Wang, Y.; Jia, C.; Fan, Z.; Lin, Z.; Lee, S. J.; Atallah, T. L.; Caram, J. R.; Huang, Y.; Duan, X. Large-Area Synthesis and Patterning of All-Inorganic Lead Halide Perovskite Thin Films and Heterostructures. *Nano Lett.* **2021**, *21* (3), 1454−1460.
(34) Kong, Q.; Lee, W.; Lai, M.; Bischak, C. G.; Gao, G.; Wong, A. B.; Lei, T.; Yu, Y.; Wang, L. W.; Ginsberg, N. S.; Yang, P. Phase-transition-induced p−n junction in single halide perovskite nanowire. *Proc. Natl. Acad. Sci. U.S.A.* **2018**, *115* (36), 8889−8894.
(35) Tang, B.; Hu, Y.; Lu, J.; Dong, H.; Mou, N.; Gao, X.; Wang, H.; Jiang, X.; Zhang, L. Energy transfer and wavelength tunable lasing of single perovskite alloy nanowire. *Nano Energy* **2020**, *71*, 104641.
(36) Huang, L.; Gao, Q.; Sun, L. D.; Dong, H.; Shi, S.; Cai, T.; Liao, Q.; Yan, C. H. Composition-Graded Cesium Lead Halide Perovskite Nanowires with Tunable Dual-Color Lasing Performance. *Adv. Mater.* **2018**, *30* (27), 1800596.
(37) Dou, L.; Lai, M.; Kley, C. S.; Yang, Y.; Bischak, C. G.; Zhang, D.; Eaton, S. W.; Ginsberg, N. S.; Yang, P. Spatially resolved multicolor $CsPbX_3$ nanowire heterojunctions via anion exchange. *Proc. Natl. Acad. Sci. U.S.A.* **2017**, *114* (28), 7216−7221.
(38) Feng, L.; Wang, Z.; Wang, W.; Li, F.; Ren, Y.; Wang, Y. Constructing Urbach-Tail-Free and Low-Threshold Perovskite Heteronanowire Lasers toward All-Optical Switching. *ACS Photonics* **2022**, *9* (2), 459−465.
(39) Hao, J.; Kim, Y. H.; Habisreutinger, S. N.; Harvey, S. P.; Miller, E. M.; Foradori, S. M.; Arnold, M. S.; Song, Z.; Yan, Y.; Luther, J. M.; Blackburn, J. L. Low-energy room-temperature optical switching in mixed-dimensionality nanoscale perovskite heterojunctions. *Sci. Adv.* **2021**, *7* (18), No. eabf1959.
(40) Lee, J. W.; Tan, S.; Han, T. H.; Wang, R.; Zhang, L.; Park, C.; Yoon, M.; Choi, C.; Xu, M.; Liao, M. E.; Lee, S. J.; Nuryyeva, S.; Zhu, C.; Huynh, K.; Goorsky, M. S.; Huang, Y.; Pan, X.; Yang, Y. Solid-phase hetero epitaxial growth of α-phase formamidinium perovskite. *Nat. Commun.* **2020**, *11* (1), 5514.
(41) Khan, R.; Chu, S.; Li, Z.; Ighodalo, K. O.; Chen, W.; Xiao, Z. High Radiance of Perovskite Light-Emitting Diodes Enabled by Perovskite Heterojunctions. *Adv. Funct. Mater.* **2022**, *32* (32), 2203650.
(42) Zhang, J.; Sun, T.; Zeng, S.; Hao, D.; Yang, B.; Dai, S.; Liu, D.; Xiong, L.; Zhao, C.; Huang, J. Tailoring neuroplasticity in flexible perovskite QDs-based optoelectronic synaptic transistors by dual modes modulation. *Nano Energy* **2022**, *95*, 106987.
(43) Chen, P.; Hu, J.; Yu, M.; Li, P.; Su, R.; Wang, Z.; Zhao, L.; Li, S.; Yang, Y.; Zhang, Y.; Li, Q.; Luo, D.; Gong, Q.; Sargent, E. H.; Zhu, R.; Lu, Z. H. Refining Perovskite Heterojunctions for Effective Light-Emitting Solar Cells. *Adv. Mater.* **2023**, *35* (3), 2208178.
(44) Mali, S. S.; Patil, J. V.; Shao, J. Y.; Zhong, Y. W.; Rondiya, S. R.; Dzade, N. Y.; Hong, C. K. Phase-heterojunction all-inorganic perovskite solar cells surpassing 21.5% efficiency. *Nat. Energy* **2023**, *8* (9), 989−1001.
(45) Su, W.; Zhang, S.; Liu, C.; Tian, Q.; Liu, X.; Li, K.; Lv, Y.; Liao, L.; Zou, X. Interlayer Transition Induced Infrared Response in ReS_2/2D Perovskite van der Waals Heterostructure Photodetector. *Nano Lett.* **2022**, *22* (24), 10192−10199.
(46) Geng, X.; Zhang, P.; Ren, J.; Dun, G. H.; Li, Y.; Jin, J.; Wang, C.; Wu, X.; Xie, D.; Tian, H.; Yang, Y.; Ren, T. L. Directly integrated mixed-dimensional van der Waals graphene/perovskite heterojunction for fast photodetection. *InfoMat* **2022**, *4* (8), No. e12347.
(47) Li, S. X.; Xia, H.; Wang, L.; Sun, X. C.; An, Y.; Zhu, H.; Bai, B. F.; Sun, H. B. Self-Powered and Flexible Photodetector with High Polarization Sensitivity Based on $MAPbBr_3$-$MAPbI_3$ Microwire Lateral Heterojunction. *Adv. Funct. Mater.* **2022**, *32* (45), 2206999.
(48) Fan, C.; Xu, X.; Yang, K.; Jiang, F.; Wang, S.; Zhang, Q. Controllable Epitaxial Growth of Core-Shell PbSe@$CsPbBr_3$ Wire Heterostructures. *Adv. Mater.* **2018**, *30* (45), 1804707.
(49) Gu, Z.; Huang, Z.; Li, C.; Li, M.; Song, Y. A general printing approach for scalable growth of perovskite single-crystal films. *Sci. Adv.* **2018**, *4* (6), No. eaat2390.
(50) Kong, L.; Zhao, Q.; Wang, H.; Guo, J.; Lu, H.; Hao, H.; Guo, S.; Tu, X.; Zhang, L.; Jia, X.; Kang, L.; Wu, X.; Chen, J.; Wu, P. Single-Detector Spectrometer Using a Superconducting Nanowire. *Nano Lett.* **2021**, *21* (22), 9625−9632.
(51) Sun, H.; Tian, W.; Cao, F.; Xiong, J.; Li, L. Ultrahigh-Performance Self-Powered Flexible Double-Twisted Fibrous Broadband Perovskite Photodetector. *Adv. Mater.* **2018**, *30* (21), 1706986.
(52) Wang, C.; Li, G.; Dai, Z.; Tian, W.; Li, L. Patterned Chiral Perovskite Film for Self-Driven Stokes Photodetectors. *Adv. Funct. Mater.* **2024**, *34*, 2316265.
(53) Lai, M.; Obliger, A.; Lu, D.; Kley, C. S.; Bischak, C. G.; Kong, Q.; Lei, T.; Dou, L.; Ginsberg, N. S.; Limmer, D. T.; Yang, P. Intrinsic anion diffusivity in lead halide perovskites is facilitated by a soft lattice. *Proc. Natl. Acad. Sci. U.S.A.* **2018**, *115* (47), 11929−11934.
(54) Baek, E.; Das, N. R.; Cannistraci, C. V.; Rim, T.; Bermúdez, G. S. C.; Nych, K.; Cho, H.; Kim, K.; Baek, C. K.; Makarov, D.; Tetzlaff, R.; Chua, L.; Baraban, L.; Cuniberti, G. Intrinsic plasticity of silicon nanowire neurotransistors for dynamic memory and learning functions. *Nat. Electron.* **2020**, *3* (7), 398−408.
(55) Lin, C. K.; Zhang, Y.; Gao, M.; Lin, J. A.; Le, H. K. D.; Lin, Z.; Yang, P. Controlling the Phase Transition in $CsPbI_3$ Nanowires. *Nano Lett.* **2022**, *22* (6), 2437−2443.
(56) Lai, M.; Lei, T.; Zhang, Y.; Jin, J.; Steele, J. A.; Yang, P. Phase transition dynamics in one-dimensional halide perovskite crystals. *MRS Bull.* **2021**, *46* (4), 310−316.
(57) Lv, Q.; Wang, X. D.; Yu, Y.; Zhuo, M. P.; Zheng, M.; Liao, L. S. Lattice-mismatch-free growth of organic heterostructure nanowires from cocrystals to alloys. *Nat. Commun.* **2022**, *13* (1), 3099.
(58) Yang, Z.; Albrow-Owen, T.; Cui, H.; Alexander-Webber, J.; Gu, F.; Wang, X.; Wu, T. C.; Zhuge, M.; Williams, C.; Wang, P.; Zayats, A. V.; Cai, W.; Dai, L.; Hofmann, S.; Overend, M.; Tong, L.; Yang, Q.; Sun, Z.; Hasan, T. Single-nanowire spectrometers. *Science* **2019**, *365* (6457), 1017−1020.
(59) Xu, J.; Rechav, K.; Popovitz-Biro, R.; Nevo, I.; Feldman, Y.; Joselevich, E. High-Gain 200 ns Photodetectors from Self-Aligned CdS-CdSe Core-Shell Nanowalls. *Adv. Mater.* **2018**, *30* (20), 1800413.
(60) Laocharoensuk, R.; Palaniappan, K.; Smith, N. A.; Dickerson, R. M.; Werder, D. J.; Baldwin, J. K.; Hollingsworth, J. A. Flow-based solution-liquid-solid nanowire synthesis. *Nat. Nanotechnol.* **2013**, *8* (9), 660−666.
(61) Dai, G.; Zou, B.; Wang, Z. Preparation and Periodic Emission of Superlattice CdS/CdS:SnS_2 Microwires. *J. Am. Chem. Soc.* **2010**, *132* (35), 12174−12175.
(62) Robinson, R. D.; Sadtler, B.; Demchenko, D. O.; Erdonmez, C. K.; Wang, L. W.; Alivisatos, A. P. Spontaneous Superlattice Formation in Nanorods Through Partial Cation Exchange. *Science* **2007**, *317* (5836), 355−358.
(63) Wu, Y.; Fan, R.; Yang, P. Block-by-Block Growth of Single-Crystalline Si/SiGe Superlattice Nanowires. *Nano Lett.* **2002**, *2* (2), 83−86.
(64) Gudiksen, M. S.; Lauhon, L. J.; Wang, J.; Smith, D. C.; Lieber, C. M. Growth of nanowire superlattice structures for nanoscale photonics and electronics. *Nature* **2002**, *415* (6872), 617−620.
(65) Ren, D.; Ahtapodov, L.; Nilsen, J. S.; Yang, J.; Gustafsson, A.; Huh, J.; Conibeer, G. J.; van Helvoort, A. T. J.; Fimland, B. O.; Weman, H. Single-Mode Near-Infrared Lasing in a GaAsSb-Based Nanowire Superlattice at Room Temperature. *Nano Lett.* **2018**, *18* (4), 2304−2310.
(66) Björk, M. T.; Ohlsson, B. J.; Sass, T.; Persson, A. I.; Thelander, C.; Magnusson, M. H.; Deppert, K.; Wallenberg, L. R.; Samuelson, L.

https://doi.org/10.1021/acsnano.4c05205
ACS Nano 2024, 18, 18022−18035

One-dimensional Steeplechase for Electrons Realized. *Nano Lett.* **2002**, *2* (2), 87−89.
(67) Gu, Z.; Zhou, Z.; Huang, Z.; Wang, K.; Cai, Z.; Hu, X.; Li, L.; Li, M.; Zhao, Y. S.; Song, Y. Controllable Growth of High-Quality Inorganic Perovskite Microplate Arrays for Functional Optoelectronics. *Adv. Mater.* **2020**, *32* (17), 1908006.
(68) Gu, Z.; Huang, Z.; Hu, X.; Wang, Y.; Li, L.; Li, M.; Song, Y. In Situ Inkjet Printing of the Perovskite Single-Crystal Array-Embedded Polydimethylsiloxane Film for Wearable Light-Emitting Devices. *ACS Appl. Mater. Interfaces* **2020**, *12* (19), 22157−22162.
(69) Wang, S.; Luo, H.; Gu, Z.; Zhao, R.; Guo, L.; Wang, N.; Lou, Y.; Xu, Q.; Peng, S.; Zhang, Y.; Song, Y. Crystal Growth Regulation of α-$FAPbI_3$ Perovskite Films for High-Efficiency Solar Cells with Long-Term Stability. *Adv. Funct. Mater.* **2023**, *33* (26), 2214834.
(70) Li, J.; Xu, J.; Bao, Y.; Li, J.; Wang, H.; He, C.; An, M.; Tang, H.; Sun, Z.; Fang, Y.; Liang, S.; Yang, Y. Anion-Exchange Driven Phase Transition in $CsPbI_3$ Nanowires for Fabricating Epitaxial Perovskite Heterojunctions. *Adv. Mater.* **2022**, *34* (19), 2109867.
(71) Zhang, Z.; Lamers, N.; Sun, C.; Hetherington, C.; Scheblykin, I. G.; Wallentin, J. Free-Standing Metal Halide Perovskite Nanowire Arrays with Blue-Green Heterostructures. *Nano Lett.* **2022**, *22* (7), 2941−2947.
(72) Tsivion, D.; Schvartzman, M.; Popovitz-Biro, R.; von Huth, P.; Joselevich, E. Guided Growth of Millimeter-Long Horizontal Nanowires with Controlled Orientations. *Science* **2011**, *333* (6045), 1003−1007.
(73) Tsivion, D.; Schvartzman, M.; Popovitz-Biro, R.; Joselevich, E. Guided Growth of Horizontal ZnO Nanowires with Controlled Orientations on Flat and Faceted Sapphire Surfaces. *ACS Nano* **2012**, *6* (7), 6433−6445.
(74) Guo, P.; Liu, D.; Shen, X.; Lv, Q.; Wu, Y.; Yang, Q.; Li, P.; Hao, Y.; Ho, J. C.; Yu, K. M. On-wire axial perovskite heterostructures for monolithic dual-wavelength laser. *Nano Energy* **2022**, *92*, 106778.
(75) Li, J.; Yang, X.; Liu, Y.; Huang, B.; Wu, R.; Zhang, Z.; Zhao, B.; Ma, H.; Dang, W.; Wei, Z.; Wang, K.; Lin, Z.; Yan, X.; Sun, M.; Li, B.; Pan, X.; Luo, J.; Zhang, G.; Liu, Y.; Huang, Y.; Duan, X.; Duan, X. General synthesis of two-dimensional van der Waals heterostructure arrays. *Nature* **2020**, *579* (7799), 368−374.
(76) Sebastian, M.; Peters, J. A.; Stoumpos, C. C.; Im, J.; Kostina, S. S.; Liu, Z.; Kanatzidis, M. G.; Freeman, A. J.; Wessels, B. W. Excitonic emissions and above-band-gap luminescence in the single-crystal perovskite semiconductors $CsPbBr_3$ and $CsPbCl_3$. *Phys. Rev. B* **2015**, *92* (23), 235210.
(77) Zhou, Z.; Cui, Y.; Deng, H.-X.; Huang, L.; Wei, Z.; Li, J. Modulation of electronic and optical properties in mixed halide perovskites $CsPbCl_{3x}Br_{3(1-x)}$ and $CsPbBr_{3x}I_{3(1-x)}$. *Appl. Phys. Lett.* **2017**, *110* (11), 113901.
(78) Evarestov, R. A.; Kotomin, E. A.; Senocrate, A.; Kremer, R. K.; Maier, J. First-principles comparative study of perfect and defective $CsPbX_3$ (X = Br, I) crystals. *Phys. Chem. Chem. Phys.* **2020**, *22* (7), 3914−3920.
(79) Xu, F.; Wei, H.; Wu, Y.; Zhou, Y.; Li, J.; Cao, B. Nonmonotonic temperature-dependent bandgap change of $CsPbCl_3$ films induced by optical phonon scattering. *J. Lumin.* **2023**, *257*, 119736.
(80) Zhang, Y.; Yang, X.; Dai, Y.; Yu, W.; Yang, L.; Zhang, J.; Yu, Q.; Dong, Z.; Huang, L.; Chen, C.; Hou, X.; Wang, X.; Li, J.; Zhang, K. Ternary $GePdS_3$: 1D van der Waals Nanowires for Integration of High-Performance Flexible Photodetectors. *ACS Nano* **2023**, *17* (9), 8743−8754.
(81) Li, L.; Wu, P.; Fang, X.; Zhai, T.; Dai, L.; Liao, M.; Koide, Y.; Wang, H.; Bando, Y.; Golberg, D. Single-Crystalline CdS Nanobelts for Excellent Field-Emitters and Ultrahigh Quantum-Efficiency Photodetectors. *Adv. Mater.* **2010**, *22* (29), 3161−3165.
(82) Zhu, Z.; Deng, W.; Li, W.; Chun, F.; Luo, C.; Xie, M.; Pu, B.; Lin, N.; Gao, B.; Yang, W. Antisolvent-Induced Fastly Grown All-Inorganic Perovskite $CsPbCl_3$ Microcrystal Films for High-Sensitive UV Photodetectors. *Adv. Mater. Interfaces* **2021**, *8* (6), 2001812.
(83) Wang, Q.; Gong, Z.; Wu, S.; Pan, S.; Pan, J. UV photodetector properties of $CsPbCl_3$ grown by Vertical Bridgman method. *J. Cryst. Growth* **2022**, *596*, 126838.
(84) Wu, X.; Sun, J.; Shao, H.; Zhai, Y.; Li, L.; Chen, W.; Zhu, J.; Dong, B.; Xu, L.; Zhou, D.; Xu, W.; Song, H.; Bai, X. Self-powered UV photodetectors based on $CsPbCl_3$ nanowires enabled by the synergistic effect of acetate and lanthanide ion passivation. *Chem. Eng. J.* **2021**, *426*, 131310.
(85) Zhang, J.; Wang, Q.; Zhang, X.; Jiang, J.; Gao, Z.; Jin, Z.; Liu, S. High-performance transparent ultraviolet photodetectors based on inorganic perovskite $CsPbCl_3$ nanocrystals. *RSC Adv.* **2017**, *7* (58), 36722−36727.

https://doi.org/10.1021/acsnano.4c05205
ACS Nano 2024, 18, 18022−18035